**Astronomy
&
Astrophysics**

Kinematic and chemical study of planetary nebulae
and H II regions in NGC 3109[*],[**]

S. N. Flores-Durán[1], M. Peña[1], and M. T. Ruiz[2]

[1] Instituto de Astronomía, Universidad Nacional Autónoma de México, Apdo. Postal 70264, 04510 Ciudad de México, Mexico
   e-mail: sflores,miriam@astro.unam.mx
[2] Depto. de Astronomía, Universidad de Chile, Casilla 36D, Las Condes, Santiago, Chile
   e-mail: mtruiz@das.uchile.cl

ABSTRACT

Aims. We present high-resolution spectroscopy of a number of planetary nebulae (PNe) and H II regions distributed along the dwarf irregular galaxy NGC 3109 and compare their kinematical behavior with that of H I data. We aim to determine if there is a kinematical connection among these objects. We also aim to determine the chemical composition of some PNe and H II regions in this galaxy and discuss it in comparison with stellar evolution models.

Methods. Data for eight PNe and one H II region were obtained with the high-resolution spectrograph *Magellan* Inamori Kyocera Echelle (MIKE) at Las Campanas Observatory, Chile. Data for three PNe, six compact H II regions, and nine knots or clumps in extended H II regions were obtained with the high-resolution spectrograph Manchester Echelle Spectrometer (MES) attached to the 2.1m telescope at the Observatorio Astronómico Nacional, SPM, B.C., Mexico. An additional object was obtained from The SPM Catalogue of Extragalactic Planetary Nebulae. Thus, in total we have high-quality data for nine of the 20 PNe detected in this galaxy, and many H II regions. In the wavelength calibrated spectra, the heliocentric radial velocities were measured with a precision better than 7.8 km s^{-1}. Data for blue supergiant stars were collected from the literature to be included in the analysis. The heliocentric radial velocities of the different objects were compared to the velocities of the H I disk at the same position. Physical conditions and ionic abundances of PNe and H II regions were obtained from the emission lines, and we used recent ionization correction factors to derive the total chemical abundances.

Results. From the analysis of radial velocities we found that H II regions in NGC 3109 share the kinematics of the H I disk at the same projected position with very low dispersion in velocities. Blue supergiant stars and PNe rotate in the same direction as the H I disk but these objects have much larger dispersion; this larger dispersion is possibly because these objects belong to a different population that is located in the central stellar bar reported for this galaxy. From the chemical abundance determinations we demonstrate that PNe are enriched in O and Ne. The average O abundance in H II regions is 12 + log O/H = 7.74 ± 0.09 and PNe show significantly higher oxygen abundance by 0.43 dex in average. Ne abundance are about three times larger in PNe than in H II regions. This is a very important result showing that because of the low metallicity in the galaxy, O and Ne in PNe have been enriched by their progenitors in nucleosynthesis processes and brought to the surface during third dredge-up events. Our PN abundances are better reproduced by some nonstandard stellar evolution models for a metallicity of $Z = 0.001$, similar to the metallicity of H II regions. Abundances in H II regions show no metallicity gradient in this galaxy. We discuss a possible connection between the kinematics and chemistry.

Key words. ISM: abundances – ISM: kinematics and dynamics – H II regions – planetary nebulae: general – Galaxy: abundances – galaxies: dwarf

1. Introduction

The analysis of extragalactic PNe kinematics allows us to trace low-intermediate mass stars kinematics. Kinematics of PNe has been studied in elliptical, spiral, and S0 galaxies for comparison with the kinematics of other stellar populations and to determine the galactic mass (see, e.g., Merrett et al. 2006; Coccato et al. 2009; Cortesi et al. 2013; Longobardi et al. 2013, and references therein). For example, M31 has been deeply analyzed by Merrett et al. (2006) who found that PNe lying close to M31 major axis show a rotation curve with a wide spread in velocities at small radii, which is indicative of a contribution from the barred bulge. By contrast, Herrmann & Ciardullo (2009) studied

550 PNe belonging to five face-on spirals (IC 342, M74, M83, M94, and M101) to determined their kinematic mass.

The kinematics of PNe in dwarf irregular galaxies has been less studied. The Local Group member IC 10 was analyzed by Gonçalves et al. (2012), who studied the relation of the PN population and the H I envelope. For this case they reported a kinematical connection between both populations. In NGC 6822, PN kinematics was analyzed by Flores-Durán et al. (2014), who found significant differences between the PNe velocities and the velocities of the H I disk at the same position. These authors reported that, in NGC 6822, PNe share the rotation of the middle-age C stars.

NGC 3109 is a Magellanic-type galaxy classified as a late spiral SB(s)m. It is the dominant member of a group of galaxies at the edge of the Local Group, which includes the irregulars Sextans A, Sextans B, and the dwarf elliptical Antlia Dwarf.

The structure of NGC 3109 is complex. In the optical it seems to contain a gas-rich rotating disk and a halo of old stars (Minniti et al. 1999). Such a disk seems to be oriented edge-on and has an elongated shape that is aligned almost E-W with an extension of about 17.4 × 3.5 arcmin. A huge disk of H I, which is aligned with the optical disk and encompasses it, was mapped by Barnes & de Blok (2001). These authors found that such a disk is warped and suggested that this could be evidence of a possible encounter with the Antlia Dwarf approximately one billion years ago. Peña et al. (2007a) reported the discovery of 20 PNe in NGC 3109 and Peña et al. (2007b) analyzed the chemistry of some of them and found that the O abundance in PNe is systematically higher than in H II regions, which is a very unusual situation.

H I disk kinematics was presented in detail by Ott et al. (2012) and analyzed extensively by Carignan et al. (2013), who extended the analysis up to a size of 58 × 27 arcmin.

Star formation has been very active in NGC 3109 as indicated by the large number of H II regions it contains. This is one of the most metal-poor galaxies in the vicinity of the Local Group with metallicity and luminosity that are lower than the values of the Small Magellanic Cloud. The main physical properties of NGC 3109 are listed in Table 1.

In this work we aim to study, in a global way, the PNe and compact H II regions in this galaxy with a twofold purpose. First we analyze the kinematics of these nebulae and compare them with the H I disk kinematics, and second, we determine chemical abundances of PNe in comparison with the abundances of H II regions to understand the chemical evolution of the central stars in a very low metallicity environment. Finally we discuss a possible relation between the kinematics of nebulae and their chemistry. The objects analyzed in this work are listed in Table 2.

A similar analysis was performed by our group in NGC 6822 (García-Rojas et al. 2016; Flores-Durán et al. 2014), where we studied the chemical behavior of photoionized nebulae and their kinematics relative to the H I disk and the huge spheroid of C stars in this galaxy. There we probed that the young population (H I and H II gas) and intermediate-age population (C stars and PNe) display different kinematics and chemistry. NGC 3109 does not possess such an extensive halo of C stars. The brightest members of such a population were studied by Demers et al. (2003) and these members are distributed in and near the disk of NGC 3109, as most of its stellar component.

This paper is organized as follows: in Sect. 2 we present the observations and data reduction, as well as the radial velocities derived for the different objects. In Sect. 3 the velocities of PNe, compact H II regions, and knots or clumps found in extended H II regions are discussed and compared to the velocities of the H I disk. In this section we also present the results of the kinematical analysis. In Sect. 4 the chemical abundances of PNe and H II regions are calculated and discussed. A discussion on a possible relation between the kinematics and chemistry in the galaxy is contained in Sect. 5. Our general conclusions are presented in Sect. 6.

2. Data acquisition and reduction

High spectral-resolution data for nine PNe (PN3, PN9, PN10, PN11, PN13, PN14, PN16, PN17, and PN20; here and in the following the object names are after Peña et al. 2007a) and one H II region were obtained with the double echelle *Magellan* Inamori Kyocera Echelle spectrograph (MIKE) attached to the 6.5 m *Magellan* Telescope Clay at Las Campanas Observatory (LCO), Chile. All but one of these objects were observed

Table 1. Physical properties of NGC 3109.

Property	Value	Ref.
Hubble type	SB(s)m	(1)
Other ID	DDO 236, UGCA 194	
RA (J2000)	10h 03m 06.9s	(1)
Dec (J2000)	−26° 09′ 34″	(1)
Distance (Mpc)	1.30 ± 0.02	(2)
Systemic Vel. (km s^{-1})	404 ± 2	(3)
PA (deg)	95.0 ± 2.0	(3)
Inclination (deg)	69.5 ± 1.5	(3)
$E(B-V)$	0.087 ± 0.012	(2)
M_V	−14.9 ± 0.1	(4)
$M_\star$ ($10^6 M_\odot$)	76	(4)
M_{HI} ($10^6 M_\odot$)	460	(3)
12 + log(O/H), H II	7.77 ± 0.07	(5)
12 + log(O/H), PN	8.16 ± 0.19	(5)
12 + log(O/H), B-type	7.76 ± 0.07	(6)
Z	0.0015	
$Z/Z_\odot$	0.13	

References. (1) de Vaucouleurs et al. (1991); NASA/IPAC Extragalactic Database; (2) Soszyński et al. (2006); (3) Carignan et al. (2013); (4) McConnachie (2012), and references therein; (5) Peña et al. (2007b); (6) B-type supergiants analyzed by Evans et al. (2007).

during the nights March 7 and 8, 2014. Another PN (PN10) was observed on May 9, 2006 (Peña et al. 2007a). The observed objects and their coordinates are listed in Table 2.

The MIKE spectrograph operates with two arms, allowing one to obtain a blue and a red spectrum simultaneously (Berstein et al. 2003). The standard set of gratings was employed, thus the wavelength coverage was from 3350 to 5050 Å in the blue and from 4950 to 9400 Å in the red. During the observing runs the seeing was better than 1″, most of the time. A binning of 2 × 2 was used obtaining a spatial scale of 0.2608″/pix. For the PNe and H II regions a slit size of 1″ × 5″ was used, thus the spectral resolution obtained was from 0.14 to 0.17 Å in the blue and from 0.23 to 027 Å in the red. Three standard stars for flux calibration were acquired (HR 4468, Hilter 600, and HD 49798) with a slit size of 2″ × 5″, to include all the stellar flux.

Several compact H II regions and PNe (listed in Table 3), and some clumps in extended H II regions, not classified previously, were observed at the Observatorio Astronómico Nacional San Pedro Mártir (OAN-SPM), B.C., Mexico, with the 2.1 m telescope and the Manchester Echelle Spectrometer (MES; Meaburn et al. 1984, 2003) in the nights February 4 to 9, 2014.

The MES (OAN-SPM) is a long-slit echelle spectrometer that uses narrowband filters to isolate the orders containing the emission lines of interest. For our observations the order including the Hα and [N II] 6548, 6583 Å emission lines was used. All the observations were made with a slit width of 150 μm, equivalent to 1.9″ on the sky. The slit length is 6.5′ and it was oriented E-W, along the disk of NGC 3109, therefore several objects and H II knots were included in the slit (see Fig. 1).

The MES (OAN-SPM) was coupled with a 2048 × 2048 pix Marconi2 CCD with 13.5 μm pixel size, binned 2 × 2. The resulting plate scale was 0.356″/pixel, and the spectral resolution, approximately of 0.10 Å/pix, was equivalent to 11 km s^{-1}. Immediately before or after every science observation, a Th−Ar lamp spectrum was obtained for wavelength calibration. The internal precision of the lamp calibrations is better than ±1.0 km s^{-1}.

Table 2. PNe[a], compact H II regions[a], and H II knots or clumps analyzed in NGC 3109.

Object	RA (2000)	Dec (2000)	Other ID
PN3[bc]	10:02:49.15	−26:09:10.1	–
PN9[bc]	10:03:02.66	−26:08:50.3	–
PN10[bc]	10:03:03.91	−26:09:42.3	PN6[d]
PN11[b]	10:03:05.04	−26:10:54.2	–
PN13[bc]	10:03:08.52	−26:09:07.7	–
PN14[b]	10:03:10.34	−26:08:06.1	–
PN16[b]	10:03:18.67	−26:09:58.8	–
PN17[b]	10:03:18.74	−26:10:05.4	–
PN20[bc]	10:03:25.51	−26:09:07.2	–
H II 4[c]	10:02:50.66	−26:09:35.9	near F2 H7[f]
H II 6[c]	10:02:52.03	−26:09:05.3	F2 H3[f]
H II 9a[c,g]	10:02:58.20	−26:08:45.8	PN7[a], PN1[d]
H II 10[c]	10:02:58.91	−26:08:48.3	RM 2[d], Ho 11[e]
H II 18[c]	10:03:03.77	−26:09:20.7	RM 6[d], D2 H5[f]
H II 30[b]	10:03:17.71	−26:09:59.4	near HII 10[d]
H II 37[c]	10:03:27.96	−26:09:19.9	–
H II 40[c]	10:03:28.51	−26:09:21.8	near F5 H4[f]
H II 41[c]	10:02:50.64	−26:08:44.0	F2 H5[f]
H II 42[c]	10:02:51.96	−26:09:24.4	F2 H6[f]
H II 43[c]	10:02:52.07	−26:09:08.1	F2 H3[f]
H II 44[c]	10:02:59.46	−26:08:48.2	–
H II 45[c]	10:02:59.47	−26:09:01.8	–
H II 46[c]	10:02:59.61	−26:08:45.6	–
H II 47[c]	10:03:03.86	−26:09:08.4	D2 H5[f]
H II 48[c]	10:03:12.45	−26:08:49.7	D2 H1[f]
H II 49[c]	10:03:27.84	−26:10:23.0	–

Notes. [(a)] Names as in Peña et al. (2007a). H II 41–49 are knots or clumps in extended H II regions. [(b)] Observed at LCO with MIKE. [(c)] Observed with MES. [(d)] Richer & McCall (1992), [(e)] Hodge (1969), [(f)] Bresolin et al. (1993). [(g)] This object, classified as a PN by Richer & McCall (1992), was finally identified as a H II region in Peña et al. (2007b), here we renamed it as H II 9a.
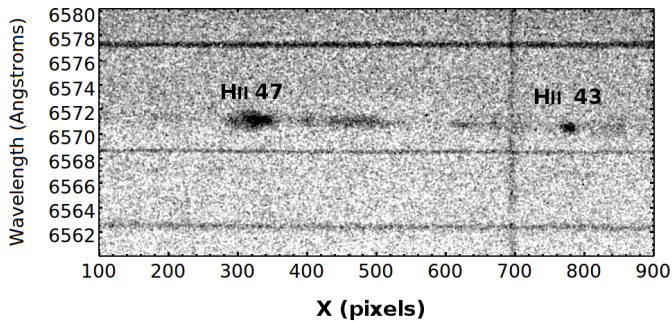

Fig. 1. Example of a Hα 2D image obtained with MES-SPM showing two H II clumps inside an extended H II region. The slit size was 1.9″ along the dispersion axis, and 6.5′ in the spatial direction, oriented E-W. The Hα emission of the galaxy shows a gradient in wavelength, relative to the sky lines, due to rotation.

The total exposure times for each object, observed with MIKE or MES, are presented in Table 3. Kinematic data for two additional objects (PN10 and H II 9a) were extracted from The San Pedro Mártir Kinematic Catalogue: Extragalactic Planetary Nebulae (SPM KINCAT) by Richer et al. (2010).

Table 3. Exposure times.

	Exp. time (s)	
id	MIKE	MES
PN3	1800	–
PN9, H II 44, H II 48	2700	900
PN10	6 × 900	3600[a]
PN11	2700	1800
PN13	1800	–
PN14	900	–
PN16	1800	–
PN17	900	–
PN20	3600	3600
H II 4, H II 41	–	3600
H II 9a	–	3600[a]
H II 6, H II 43	–	3600
H II 10, H II 45, H II 46	–	1800
H II 18	–	1800
H II 30	900	–
H II 37, H II 49	–	1200
H II 40	-	1800
H II 42, H II 47	–	1800

Notes. [(a)] Data from SPM KINCAT of PNe.

2.1. Data reduction

Data reduction of LCO Clay-MIKE spectra was carried out with IRAF[1] echelle reduction packages. Data were bias subtracted and flat fielded. Spectra were extracted from the 2D frames with an extraction window of 3.13″, which includes all the emission of stellar objects and an important fraction (if not all) of the emission of compact H II regions. Wavelength calibration was performed with a Th−Ar lamp, observed immediately after each science exposure. The flux calibration was carried out employing the spectrophotometric standard stars mentioned above.

The data from MES (OAN-SPM) were reduced via the noao.twodspec.longslit package of IRAF. First, 2D frames were bias substracted and second, the data were extracted and wavelength-calibrated using a Th−Ar lamp. No flat-field correction was applied. The fits files retrieved from the SPM KINCAT provide wavelength-calibrated spectra. These data are not flux calibrated. The heliocentric velocity correction was applied for all the spectra.

3. Radial velocities

In this section the radial velocity behavior of our objects is analyzed and compared with the velocities of the H I disk at the same projected position.

3.1. The H I disk

Detailed observations with high-velocity resolution (0.6–2.6 km s⁻¹) of neutral hydrogen (H I) emission were obtained by Ott et al. (2012) with the VLA-ANGST (Very Large Array survey of Advanced Camera for Surveys Nearby Galaxy Survey Treasury galaxies) for 35 nearby dwarf galaxies, including NGC 3109. It is possible to access their data on the web site[2].

---

[1] IRAF is distributed by the National Optical Astronomy Observatories, which is operated by the Association of Universities for Research in Astronomy, Inc., under contract to the National Science Foundation.
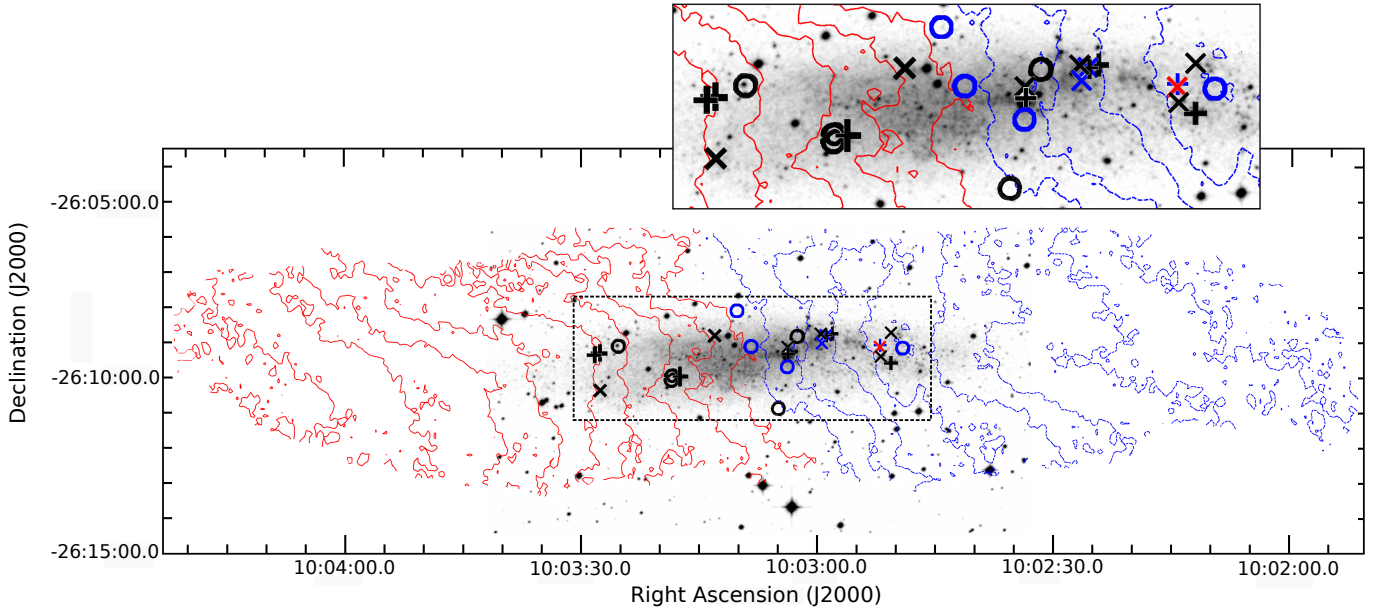[2] https://science.nrao.edu/science/surveys/vla-angst

Fig. 2. Moment map of the H I in NGC 3109 (Ott et al. 2012). The blue contours run from 400 km s^{-1} in the center to 351 km s^{-1} in the west in steps of 7 km s^{-1}. Red contours run from 407 km s^{-1} in the *inner zone* to 463 km s^{-1} in the east. Positions of analyzed PNe (circles), H II regions (crosses), and H II knots (x symbols) are shown. Blue symbols indicate a negative difference and red symbols indicate a positive difference (larger than 12 km s^{-1}) between the observed objects and the H I velocities. We plot, in black, objects with a difference in velocity lower than 12 km s^{-1}, relative to H I disk.

Figure 2 is based on the H I data by Ott et al. (2012). This figure shows some interesting characteristics of the isovelocity contours of the H I disk, especially in the central zone. These contours are almost parallel to each other and almost orthogonal to the main axis of the disk, giving the appearance of a nearly solid-body type rotation. In addition it is clear that the H I disk is much larger in size than the optical galaxy, where the stars and the ionized gas reside. We refer to this in the following.

Previous to Ott et al. (2012), Jobin & Carignan (1990) obtained H I 21-cm line observations with the Very Large Array (VLA), and they constructed a position-velocity diagram from which they derived the rotation curve (RC) out to about 17 arcmin from the center; this is equivalent to 6 kpc if a distance of 1.3 Mpc is adopted. This early study reported a slowly rising RC, reaching a maximum rotational velocity of only 67 km s^{-1}. In addition, from surface photometry in the *I* band, these authors found that the orientation of the isophotes changes, giving strong evidence for the presence of a bar in NGC 3109.

Blais-Ouellette et al. (2003) combined high-resolution Fabry-Perot Hα emission, which is confined to the optical zone, with the H I 21-cm data to compute the RC. They showed that the ionized gas of NGC 3109 and the H I share the same kinematics. Their computed RC presents a nearly solid-body type behavior rising linearly and slowly up to a velocity of about 45 km s^{-1} at 2.5 kpc and then it rises more slowly getting 65 km s^{-1} at a distance of about 7 kpc from the center.

As mentioned in the introduction, Carignan et al. (2013) reported a H I disk of 58 × 27 arcmin in size, which is approximately four times larger than the optical disk. The RC calculated by Carignan et al. (2013) coincides very well with the RC derived by previous authors and it shows that the rotation velocity continues slowly increasing up to 12 kpc, where it gets a value of about 80 km s^{-1}. In addition, these authors analyzed the H I isophotes and photometric distribution in the *B*, *I*, and

3.6 μm bands, which are sampling different stellar populations; they found that the inclination and thickness of the disk changes with each band and that the H I disk is really composed of two disks with different inclinations.

Jobin & Carignan (1990), Blais-Ouellette et al. (2003), and Carignan et al. (2013) used the RC to model the mass distribution of the dark matter (DM) halo in the galaxy. Such models led the authors to conclude that NGC 3109 is entirely dominated by DM at nearly all radii. According to these authors, the model that best fit the RC is the observationally motivated pseudo-isothermal (ISO) DM halo with a flat-density core profile, contrary to the cosmological Navarro-Frenk-White models which predict a cuspy central halo for these type of galaxies. It is worthwhile to say that such a galaxy dominated by DM at all radii could not produce a bar since bars are formed by barionic matter (stars) and can be formed if the barionic matter centrally dominates (see references below).

A cosmologically motivated model for the DM halo distribution, containing a cuspy central DM density, was computed by Valenzuela et al. (2007) for NGC 3109. The DM component is globally dominant but the model is centrally dominated by barions, therefore it is unstable to bar formation. The best model by Valenzuela et al. (2007) develops a weak stellar bar that extends in radius to about 1 kpc, in about 100 Myr. The idea of a barred galaxy is supported by the change in orientation of the isophotes shown in the surface photometry (Jobin & Carignan 1990).

3.2. Is there a bar in the central zone of NGC 3109?

Several authors have suggested that NGC 3109 is a barred galaxy (see, e.g., the classification by de Vaucouleurs et al. 1991). As described above, the twist of the stellar isophotes in the *B* and *I* bands (Jobin & Carignan 1990) supports the idea of a barred galaxy. However a DM centrally dominated galaxy, as
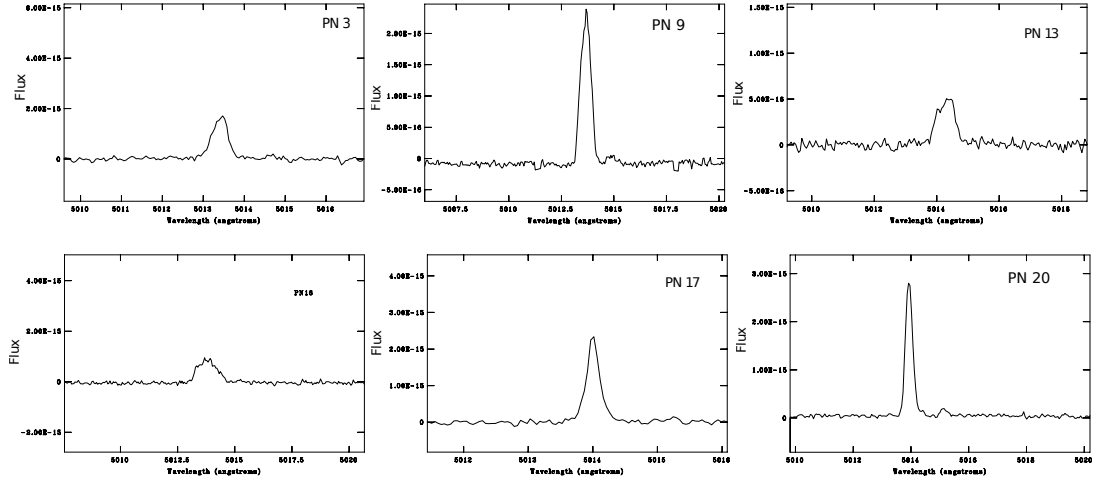
Fig. 3. [O III]λ5007 emission lines of PNe from the spectra obtained with MIKE spectrograph at LCO.
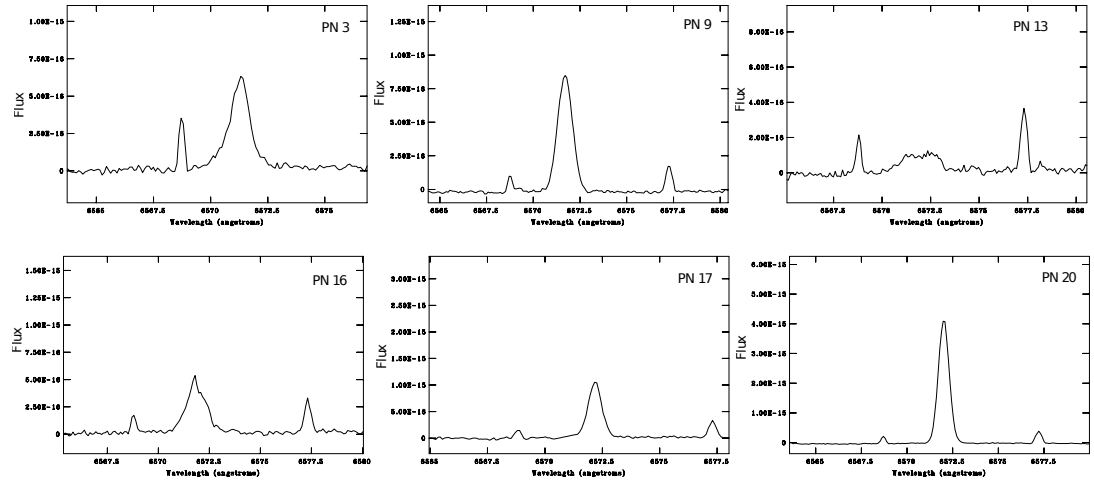

Fig. 4. Hα and [N II] emission lines of PNe from the spectra obtained with MIKE spectrograph at LCO.

the ISO model computed by, for example, Carignan et al. (2013), would not develop a bar. The physical reasons why a DM centrally dominated galaxy does not develop a bar can be found in Weinberg (1985), Debattista & Sellwood (2000), and references therein. Only the cosmological DM models by Valenzuela et al. (2007) predict the presence of a bar of 1 kpc long, which is small compared with the size of the optical zone in NGC 3109 of about 5 kpc.

The kinematics of a bar-like structure should be reflected in the RC as a linear increase in velocity. This agrees with the RC by Blais-Ouellette et al. (2003) for the ionized and neutral gas in the center. The RC increases linearly reaching 40 km s^{-1} at 2.5 kpc from the center and beyond this point it increases more slowly.

Therefore the evidence for a central bar seems solid. Such a structure would rotate with a linear RC, but the components would rotate in different directions inside the bar, showing a dispersion in velocities. Our PNe, as pertaining to the middle-age stellar population would be part of the bar and their kinematics could show this fact. But there are only nine objects and it is difficult to extract valid conclusions, therefore for the analysis we include the kinematical data for other stellar components, which are the blue supergiant stars studied by Evans et al. (2007).

3.3. Kinematics of PNe, compact H II regions, and blue supergiant stars

Several emission lines were measured in the MIKE high-resolution spectra of the observed nebulae to determine their radial velocities. In Figs. 3 and 4, the [O III] λ5007 and Hα and [N II] line profiles, obtained with this instrument, are presented. In the case of MES (OAN-SPM) data, Hα line was used to determine the observed objects velocities.

For all cases, radial velocities were calculated by a Gaussian fit to the emission lines, and they were corrected to heliocentric velocities, V_{helio}. The uncertainties listed in Table 4 correspond to the standard deviation of the measurements. For some PNe we have independent observations with both instruments and we find that the differences in radial velocities are less than 6 km s^{-1} between both sets of observations. We therefore conclude that our radial velocities have an absolute precision better than the maximum error found which is 7.8 km s^{-1}.

Using the H I disk velocity field, we compared V_{helio} of PNe and H II regions with those of the H I gas at the same projected position. The results are shown in Table 4 where we present, for all our objects, the derived V_{helio} and its uncertainty at 1σ (Cols. 2 and 3), and the H I velocity (Col. 4) at the corresponding

Table 4. Heliocentric velocities of PNe, H II regions (Col. 12), and the H I gas at the same projected position.

Object	V_{helio} km s^{-1}	±error km s^{-1}	V_{HI} km s^{-1}	Δ km s^{-1}	Δ_{sys} km s^{-1}
PN3	376.4	6.0	371.8	−4.6	−27.6
PN9	402.4	3.9	394.1	−8.3	−1.6
PN10	409.0	2.0	396.5	−12.5	+5
PN11	403.8	3.4	403.3	−0.5	−0.2
PN13	429.5	2.1	405.8	−23.7	+25.5
PN14	465.2	7.8	405.3	−59.9	+61.2
PN16	412.3	5.2	418.1	+5.8	+8.3
PN17	426.4	1.5	418.7	−7.6	+22.4
PN20	424.7	4.5	430.1	+5.4	+20.7
H II 4	385.3	0.1	377.9	−7.4	−18.7
H II 9a	385.7	0.4	386.6	+0.9	−18.3
H II 6	390.5	0.1	375.9	−14.6	−13.5
H II 10	392.8	0.5	385.7	−7.1	−11.3
H II 18	395.3	0.1	396.7	+1.4	−8.7
H II 30	411.8	2.5	415.5	+3.7	+7.8
H II 37	428.9	0.2	434.1	+5.2	+24.9
H II 40	426.5	0.1	434.6	+8.1	+22.5
H II 41	375.7	0.1	377.0	+1.3	−28.4
H II 42	369.3	0.1	379.9	+7.6	−34.8
H II 43	356.9	0.1	375.7	+18.8	−47.1
H II 44	405.3	0.2	386.3	−19.1	+1.3
H II 45	408.3	0.4	389.3	−19.0	+4.3
H II 46	382.9	0.5	389.0	+6.1	−21.1
H II 47	388.3	0.1	395.3	+7.0	−15.8
H II 48	422.4	0.6	411.7	−10.7	+18.4
H II 49	424.1	0.6	431.7	+7.6	+20.1

Notes. Δ and Δ_{sys} are the differences $V_{HI} - V_{helio}$ and $V_{helio} - V_{sys}$, respectively.

position. Column 5 shows the difference $\Delta = V_{HI} - V_{helio}$, and in Col. 6 we present the difference between the observed velocity and systemic velocity (404 km s^{-1}).

The projected position of observed objects and their differences in velocity, relative to the H I disk, are illustrated in Fig. 2, where the velocity map of H I, as given by Ott et al. (2012), is shown. The difference in velocity of PNe and H II regions is indicated in blue or red if it is negative (objects approaching faster by more than 12 km s^{-1}) or positive (objects receding by more than 12 km s^{-1}), with respect to the H I disk. Objects with differences smaller than ±12 km s^{-1} are shown in black.

To better illustrate the differences in velocity among PNe, compact H II regions and knots in H II regions, and the H I disk, Fig. 5 shows their velocities (relative to the systemic velocity) versus their distance to the center (in kpc) projected along the major axis of the H I disk. Only the inner 5 kpc of the galaxy, where the stars and the ionized gas reside, are shown. The filled blue line represents the rotation of the H I disk and it shows some irregularities that so far have not been explained. At both sides of this line two dotted lines show the uncertainty given by Ott et al. (2012). From this figure the velocity gradient, at both sides of the center, can be calculated. We find that from the galactic center to the east the rotation velocity increases by 17.4 km s^{-1} kpc^{-1}, while from the center to the west, the velocity declines by 15.3 km s^{-1} kpc^{-1}. Both gradients are equal within the uncertainties given by the dotted lines.

In this figure it is clear that our H II regions (open squares) follow closely the rotation of the H I disk, this is in agreement with the results found by Blais-Ouellette et al. (2003) for the ionized gas. We find that the PNe (black dots) also rotate in the same
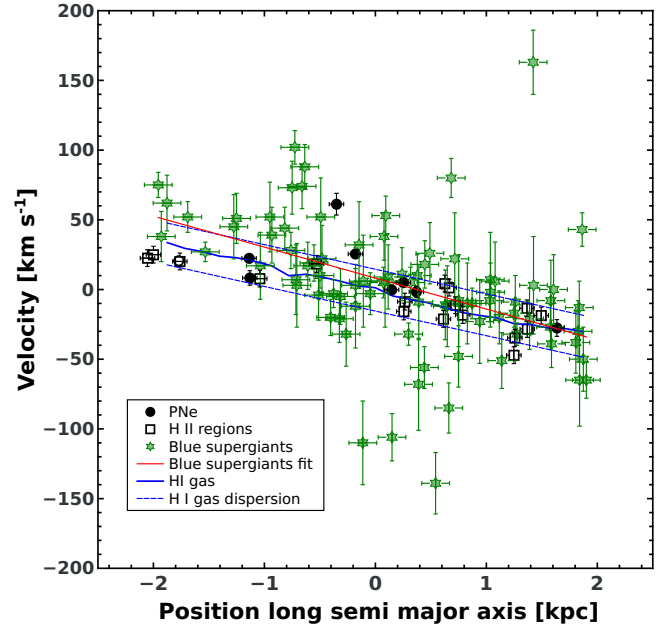
Fig. 5. Velocities of PNe, H II regions, and BSGs relative to the system versus their positions relative to the center, projected on the H I disk major axis. Solid and dotted blue lines show the rotation of the H I disk and its dispersion. The red line is a fit to the BSG velocities.

direction as the disk, although these objects present a much more disperse velocity field. One PN in particular shows a difference of about 60 km s^{-1}, relative to the system and to the H I disk; the projected location of this PN (PN14) is farthest away from the H I disk.

In the same figure, we included the radial velocities, relative to the system, of luminous blue supergiant stars (BSGs, green stars) as determined by Evans et al. (2007) from multiobject spectroscopy, although their data have lower resolution than the data in this work. The uncertainty given by Evans et al. (2007) for each object is shown; the mean uncertainty is of 19 km s^{-1}. The projected position of these objects along the major axis of the H I disk was calculated. As already indicated by Evans et al. (2007), the BSGs, that are relatively young objects and would belong to the stellar bar, show a rotation in the same direction as the H I rotation but with a large dispersion, even larger than that presented by our PN sample. If we trace a linear fit to the BSG data, a slightly steeper line is found (red line in Fig. 5). However, given the lower accuracy of the data for the BSGs, we consider that this small difference is not trustworthy. The distribution of BSGs in the galaxy (see Figs. 2 and 3 by Evans et al. 2007) spreads in a thicker zone than that of the H II regions, which also occurs with the distribution of PN candidates as presented by Peña et al. (2007a) in their Fig. 3. In our Fig. 2 this is not noticeable because only the objects analyzed in this paper are included there, and not the entire PN sample. It is clear that, from their distribution, BSGs and PNe represent different populations than the ionizing stars of H II regions.

4. Chemical abundances revisited

To analyze the chemical behavior of the photoionized nebulae in NGC 3109, we first need to calculate the physical conditions (electron temperature and density) and then the ionic abundances of elements present in the gas. In Table 5 we present dereddened line intensities for each object observed with MIKE-LCO. The

Table 5. Dereddened line intensities measured from MIKE spectra relative to Hβ = 1.00.

Ion	λ	$f(\lambda)$	PN3 I/I(Hβ)	err	PN9 I/I(Hβ)	err	PN11 I/I(Hβ)	err	PN13 I/I(Hβ)	err	PN14 I/I(Hβ)	err
[O II]	3726.03	+0.280	–	–	–	–	–	–	–	–	–	–
[O II]	3728.82	+0.279	–	–	–	–	–	–	–	–	–	–
[Ne III]	3868.75	+0.241	–	–	0.37	0.13	0.82	0.15	–	–	–	–
Hϵ	3970.07	+0.214	–	–	–	–	0.47	0.61	–	–	–	–
Hδ	4101.74	+0.179	–	–	0.28	0.09	0.32	0.09	–	–	–	–
Hγ	4340.47	+0.119	–	–	0.45	0.09	0.45	0.07	–	–	–	–
[O III]	4363.21	+0.114	–	–	<0.06	–	0.11	0.06	–	–	–	–
He II	4685.68	+0.114	–	–	0.34	0.06	–	–	–	–	–	–
Hβ	4861.33	0	1.00	0.22	1.00	0.15	1.00	0.11	1.00	0.40	1.00	0.17
[O III]	4958.91	–0.021	0.77	0.13	1.65	0.24	2.92	0.32	1.11	0.50	–	–
[O III]	5006.84	–0.031	2.99	0.43	5.17	0.61	8.89	0.99	2.33	0.40	–	–
[Ar III]	5191.82	–0.069	–	–	–	–	0.09	0.02	–	–	–	–
He I	5875.64	–0.194	–	–	–	–	–	–	–	–	–	–
[N II]	6548.03	–0.298	–	–	0.12	0.05	0.05	0.02	–	–	–	–
Hα	6562.82	–0.301	2.87	0.33	2.86	0.33	2.91	0.31	2.73	0.40	2.60	0.66
[N II]	6583.41	–0.304	0.19	0.13	0.30	0.05	0.07	0.01	–	–	–	–
[S II]	6716.47	–0.323	0.53	0.30	0.20	0.04	–	–	–	–	–	–
[S II]	6730.85	–0.325	0.24	0.08	0.16	0.03	–	–	–	–	–	–
He I	7065.28	–0.369	–	–	–	–	0.15	0.03	–	–	–	–
[Ar III]	7135.78	–0.378	–	–	0.13	0.09	–	–	–	–	–	–
c(Hβ)			0.7		0.09		0.41		–		–	
log F(Hβ)			–15.58		–15.55		–15.47		–16.03		–16.41	

Ion	λ	$f(\lambda)$	PN16 I/I(Hβ)	err	PN17 I/I(Hβ)	err	PN20 I/I(Hβ)	err	H II 30 I/I(Hβ)	err
[O II]	3726.03	+0.280	–	–	–	–	1.35	0.21	1.69	0.31
[O II]	3728.82	+0.279	–	–	–	–	1.86	0.28	2.11	0.32
[Ne III]	3868.75	+0.241	–	–	–	–	0.11	0.04	–	–
Hϵ	3970.07	+0.214	–	–	–	–	0.20	0.06	–	–
Hδ	4101.74	+0.179	–	–	–	–	0.31	0.05	0.31	0.09
Hγ	4340.47	+0.119	0.34	0.09	0.45	0.13	0.47	0.06	0.52	0.08
[O III]	4363.21	+0.114	<0.06	–	<0.03	–	<0.02	–	–	–
He II	4685.68	+0.114	–	–	–	–	–	–	–	–
Hβ	4861.33	0	1.00	0.23	1.00	0.17	1.00	0.11	1.00	0.13
[O III]	4958.91	–0.021	1.81	0.36	0.78	0.11	0.33	0.04	0.28	0.05
[O III]	5006.84	–0.031	5.26	0.74	2.20	0.26	0.95	0.11	1.05	0.13
[Ar III]	5191.82	–0.069	–	–	–	–	–		–	–
He I	5875.64	–0.194	–	–	–	–	0.04	0.01	–	–
[N II]	6548.03	–0.298	–	–	–	–	0.05	0.01	–	–
Hα	6562.82	–0.301	2.86	0.36	2.87	0.35	2.90	0.30	2.96	0.31
[N II]	6583.41	–0.304	0.08	0.03	0.19	0.04	0.17	0.02	0.09	0.03
[S II]	6716.47	–0.323	0.16	0.10	–	–	0.18	0.02	0.12	0.02
[S II]	6730.85	–0.325	0.11	0.07	–	–	0.14	0.02	0.07	0.01
He I	7065.28	–0.369	–	–	–	–	–	–	–	–
[Ar III]	7135.78	–0.378	–	–	–	–	0.06	0.01	0.04	0.04
c(Hβ)			0.03		0.05		0.28		0.79	
log F(Hβ)			–15.68		–15.58		–15.05		–15.02	

table includes the logarithmic reddening correction, c(Hβ), and the Hβ observed flux, F(Hβ). The value c(Hβ) was derived from the Balmer ratio Hα/Hβ, by assuming case B recombination theory (Storey & Hummer 1995), the reddening law by Seaton (1979), and an electron temperature of 10^4 K. Uncertainties correspond to the standard deviation of the Gaussian fit for the line, plus 10% due to possible errors in the flux calibration procedure. In the third column we present the reddening function used. We used IRAF V2.16 for data reduction and analysis.

Owing to the faintness of these objects, the temperature sensitive [O III]$\lambda\lambda$4363/5007 line ratio was obtained in very few objects. Hence we recalculated physical conditions and ionic abundances of PNe and H II regions using the line intensities given by Peña et al. (2007b), which were acquired from observations

performed with FORS1 spectrograph attached to the Very Large Telescope (ESO-VLT) in 2006. The calculations were obtained using the IRAF tasks TEMDEN and IONIC in the STSDAS package.

Electron temperatures (T_e) were derived from [O III]$\lambda\lambda$4363/5007 line ratios and electron densities (n_e), from the density-sensitive [S II]$\lambda\lambda$6717/6731 line ratios. When such [S II] line ratios were not available a density of 500 cm^{-3} was chosen for PNe and of 100 cm^{-3} for H II regions. We adopted the simplistic assumption that n_e is uniform in the nebula and equal to the value given by the [S II]$\lambda\lambda$6717/6731 ratio. We also assumed that T_e is uniform and equal to that given by the [O III]$\lambda\lambda$4363/5007 line ratio. Derived values are listed in Table 6.

Table 6. Electron temperatures, densities, and ionic abundances (10^{-6}).

	n_e (cm^{-3})	T_e(K)	He$^+$	He^{++}	O$^+$	O^{++}	N$^+$	Ne^{++}	S$^+$	Ar^{++}
PN3	140^{+800}_{-40}	$12\,013^{+1349}_{-1389}$	0.116	<0.003	8.2	110.6	0.99	19.28	0.11	0.24
PN4	500	$11\,846^{+897}_{-1276}$	<0.029	0.071	<2.70	116.6	<0.78	26.60	<0.20	–
PN9^a	213^{+14}_{-22}	$<12\,336^{+643}_{-517}$	–	–	–	94.12	3.53	17.14	0.536	0.757
PN10	500	$10\,588^{+944}_{-1128}$	0.072	<0.005	<10.5	208.6	0.85	25.04	<0.25	0.48
PN11	500	$13\,495^{+1463}_{-1664}$	0.095	<0.003	–	125.3	0.78	18.27	<0.06	0.19
PN11^a	500	$12\,387^{+1806}_{-2587}$	–	–	–	159.5	0.82	37.43	–	–
PN13	500	$16\,484^{+4834}_{-3772}$	0.141	<0.018	<2.27	119.8	2.03	9.82	–	–
PN16^a	310^{+35}_{-50}	$12\,110^{+1280}_{1120}$	–	–	–	100.9	0.98	–	0.47	–
PN17	480^{+20}_{-30}	$12\,536^{+1278}_{-2082}$	0.085	<0.003	5.68	69.9	1.48	3.07	<0.09	0.11
PN20^a	169^{+8}_{-10}	$14\,345^{+790}_{-637}$	0.029	–	31.82	11.38	1.45	3.03	0.35	0.26
H II 4	100^{+10}_{-10}	$16\,489^{+1366}_{-1976}$	0.082	–	–	20.4	0.9	2.5	0.30	0.22
H II 7	100^{+40}_{-10}	$15\,295^{+1157}_{-1107}$	0.082	–	13.7	31.6	0.6	4.3	0.24	0.30
H II 9^a	520^{+1480}_{-420}	$15\,542^{+1298}_{-1542}$	0.097	–	7.81	54.5	0.6	8.8	0.12	–
H II 11	120^{+350}_{-20}	$14\,738^{+2068}_{-2021}$	0.090	–	22.0	28.4	0.9	3.4	0.36	–
H II 15	100	$13\,795^{+2259}_{-1741}$	0.104	–	18.5	47.1	1.2	6.9	0.58	–
H II 17	–	$14\,040^{+2236}_{-2464}$	0.084	–	20.5	34.5	1.1	2.9	–	–
H II 20	100	$13\,517^{+1499}_{-1733}$	0.108	–	20.7	55.1	1.1	5.3	0.37	–
H II 30	120^{+610}_{-20}	$11\,877^{+3196}_{-4428}$	0.082	–	33.9	30.8	1.0	4.0	0.36	0.31
H II 32	100	$13\,491^{+1135}_{-914}$	0.078	–	20.7	28.8	1.7	4.8	0.56	0.36
H II 37	100	$13\,689^{+1018}_{-1183}$	0.079	–	17.9	55.2	0.5	6.4	0.22	–
H II 40	160	$13\,682^{+1340}_{-1208}$	0.078	–	11.7	40.1	0.5	5.3	0.16	–

Notes. $^{(a)}$ From data obtained with MIKE spectrograph at LCO.

Ionic abundances were derived from the following line intensities: He I $\lambda5876$, He II $\lambda4686$, [O II]$\lambda3727$, [O III]$\lambda5007$, [N II]$\lambda6583$, [Ne III]$\lambda3869$, [S II]$\lambda6717+6731$, [Ar III]$\lambda7135$, relative to Hβ, and the physical conditions described above. When a line was not detected, its upper limit was used to compute an upper limit for the corresponding ionic abundance. The results are presented in Table 6.

To derive total abundances it is necessary to take unseen ions into account. Usually this correction is performed by means of ionization correction factors (ICFs). In this work, for PNe we use the expressions recently published by Delgado-Inglada et al. (2014; D-I.14) instead of those by Kingsburg & Barlow (1994; K&B), used by Peña et al. (2007b). The ICFs by D-I.14 represent an improvement relative to K&B ICFs because they are based on a huge number of photoionization models that explore a wide space of parameters and use the most updated atomic parameters and atomic physics, and they were successfully compared with observations. The ionic abundances listed in Table 6 were used. Total abundances derived this way are presented in Table 7. In most of the cases, D-I.14 ICFs can be applied; however, PN9 and PN11 show $\omega = $ O^{2+}/(O$^+$ + O^{2+}) ≥ 0.95, which is out of the validity range of such ICFs. A different procedure, described below, was used for these objects.

To evaluate the differences between D-I.14 ICFs and K&B ICFs, we applied the latter to the data in Table 6 to determine total abundances. It is found that differences in O/H abundances are lower than 0.05 dex, for N/H abundances differences are lower than 0.1 dex, and for Ne/H abundances differences are lower than 0.08 dex. Ar/H abundances however could present large differences up to 0.3 dex and S/H abundances show differences up to 0.35 dex.

Then, at least for N, O, and Ne, K&B ICFs can be used for those objects where D-I.14 ICFs are not valid. First let us

consider the case of PN11, this is a high excitation nebula for which only O^{2+} was detected. Owing to its high excitation we can consider that O$^+$ abundance is very low, and if we take into account that He II $\lambda4686$ was not detected, then no O^{3+} is expected in this nebula. Hence it can be assumed that the total O abundance is slightly higher than the O^{2+} abundance. Under these considerations, it is obtained that $12 + \log$ O/H $\sim 8.20 \pm 0.10$ for PN11, which is, within uncertainties, similar to the value derived from VLT-FORS1 data of the same object. Ne and Ar were derived using K&B ICFs. Similar methods were used for PN9 and PN16.

The case of PN20 is different. This object is a very low excitation nebula where O^{2+} abundance is lower than O$^+$ abundance. Then its total O abundance is simply the addition of these two ionic abundances. Other elemental abundances were calculated with K&B ICFs. In following sections we argue that this object is more probably a H II region.

K&B ICFs were used for determining total abundances in H II regions.The total abundances calculated for the 8 PNe and 12 H II regions (PN20 is considered a H II region) are listed in Table 7. Their behavior is shown in Figs. 6–8, which are discussed in the following.

4.1. Oxygen abundances

Peña et al. (2007b) reported that O abundances in PNe of NGC 3109 are larger, by 0.39 dex on average, than those found in H II regions. In this work, for a larger sample of objects, we found that the average difference in O abundances is 0.43 dex larger for PNe than for H II regions, for which the average $12 + \log$ O/H value is 7.74 ± 0.09. Then, we confirmed that PNe in NGC 3109 are O rich compared to the present ISM, represented by H II regions. Interestingly, Evans et al. (2007) found

Table 7. Chemical abundances for the PNe and H II regions in NGC 3109.

	He/H	$12 + \log(\text{O/H})$	$12 + \log(\text{N/H})$	$12 + \log(\text{Ne/H})$	$12 + \log(\text{S/H})$	$12 + \log(\text{Ar/H})$
PN3	0.119 ± 0.032	8.08 ± 0.05	7.25 ± 0.25	7.31 ± 0.25	6.51 ± 0.29	5.57 ± 0.16
PN4	0.101 ± 0.009	8.48 ± 0.29	<7.80	7.86 ± 0.16	–	–
PN9[a]	–	$>7.97^b$	–	$7.23{:}^b$	–	$6.15{:}^b$
PN10	0.077 ± 0.023	8.36 ± 0.13	7.29 ± 0.23	7.42 ± 0.23	6.75 ± 0.13	5.63 ± 0.18
PN11	0.098 ± 0.051	8.09 ± 0.05	–	–	–	$5.55^b \pm 0.20$
PN11[a]	0.098 ± 0.051	$8.20^b \pm 0.10$	–	$7.57^b \pm 0.10$	–	–
PN13	0.158 ± 0.074	8.12 ± 0.20	8.06 ± 0.39	7.02 ± 0.39	–	–
PN16[a]	–	> 8.00	–	–	–	–
PN17	0.088 ± 0.022	7.89 ± 0.11	7.37 ± 0.24	6.50 ± 0.26	$<6.56 \pm 0.20$	5.42 ± 0.32
PNe statistics[c]	0.096 ± 0.030	8.17 ± 0.17	7.49 ± 0.28	7.27 ± 0.30	6.61 ± 0.20	5.67 ± 0.12
PN20[a,d]	>0.029	7.64 ± 0.15	6.29 ± 0.20	6.90 ± 0.21	6.35 ± 0.25	5.69 ± 0.14
H II 4	0.082 ± 0.013	>7.29	–	6.36 ± 0.13	–	5.59 ± 0.10
H II 7	0.082 ± 0.018	7.60 ± 0.11	6.31 ± 0.11	6.75 ± 0.12	6.29 ± 0.09	5.76 ± 0.10
H II 9a	0.098 ± 0.023	7.80 ± 0.25	6.67 ± 0.10	7.00 ± 0.08	6.14 ± 0.21	–
H II 11	0.090 ± 0.026	7.67 ± 0.16	6.32 ± 0.21	6.74 ± 0.24	6.39 ± 0.14	–
H II 15	0.104 ± 0.031	7.80 ± 0.20	6.63 ± 0.15	6.95 ± 0.23	6.68 ± 0.14	–
H II 17	0.084 ± 0.030	7.72 ± 0.21	6.50 ± 0.22	6.63 ± 0.26	–	–
H II 20	0.108 ± 0.024	7.86 ± 0.15	6.62 ± 0.18	6.82 ± 0.23	6.48 ± 0.13	–
H II 30	0.082 ± 0.030	7.79 ± 0.27	6.32 ± 0.39	6.92 ± 0.54	6.41 ± 0.38	5.76 ± 0.41
H II 32	0.078 ± 0.014	7.66 ± 0.11	6.61 ± 0.11	6.89 ± 0.20	6.61 ± 0.09	5.86 ± 0.12
H II 37	0.079 ± 0.013	7.85 ± 0.11	6.36 ± 0.15	6.90 ± 0.15	6.31 ± 0.10	–
H II 40	0.078 ± 0.013	7.70 ± 0.13	6.31 ± 0.13	6.81 ± 0.14	6.13 ± 0.10	–
H II statistics	0.088 ± 0.026	7.74 ± 0.09	6.45 ± 0.14	6.80 ± 0.13	6.38 ± 0.15	5.73 ± 0.08

Notes. [a] From data obtained with MIKE spectrograph at LCO. [b] ICFs from Kingsburgh & Barlow (1994). [c] PN11[a] is not included in the statistics. [d] PN20 is reclassified as a H II region.

that the O abundance in their sample of eight B-type supergiant stars, also a young population, is similar to the value for H II regions (see Table 1) and therefore lower than the O abundances in PNe.

In our average values for PNe we did not consider PN20 (shown as an open circle in the diagrams), which appears as a very low excitation nebula (different from what is expected for a PN) with low O abundance. Owing to its spectral characteristics and its chemistry, this nebula appears more similar to a H II region than to a PN. PN20 was classified as a PN because of its stellar appearance and low luminosity central star (Peña et al. 2007a), but in the following we consider it to be a compact H II region and place it outside the statistics for PNe.

The O enrichment of PNe relative to H II regions is a very important result, which makes evident that O (and also Ne as we will discuss later) has been synthesized and dredged up to the stellar surface during the evolution of the progenitors of these PNe. The nucleosynthesis of fresh ^{16}O is produced via the reaction ^{12}C$(\alpha, \gamma)^{16}$O and, according to some stellar evolution models (see, e.g., Marigo 2001), surface O enrichment occurs in low metallicity stars with initial mass lower than ~3.5 $M_\odot$, as a consequence of dredge-up events during the thermal pulses in the AGB phase. This O enrichment becomes negative at higher masses because of hot bottom burning (HBB), phenomenon where extra N enrichment is produced through envelope-burning conversion to N of dredged-up primary C.

Our results constitute crucial evidence confirming that low-intermediate mass stars may produce positive yields of oxygen. In the next sections we discuss our results in comparison with the predictions of some stellar evolution models for low-intermediate mass stars.

In Figs. 6 and 7, which are discussed in detail later, standard stellar evolution models by Karakas (2010, K10) and Fishlock et al. (2014, F14), and nonstandard models by

Ventura et al. (2013, 2014b, V1314), and Ventura et al. (2014a, V14) are presented. These models represent the evolution of stars with different initial masses at different initial metallicities, and model values correspond to the surface stellar abundances at the end of the AGB phase.

We consider that the best models for our objects are those with the metallicity of the ISM in NGC 3109, reproducing well the chemical composition of our PNe sample. For the case of O, it is evident that some models by K10, with very low metallicity $Z = 0.0001$, show large enrichment for stars of initial masses, at the ZAMS, from 1.5 to 3 $M_\odot$. But no enrichment (or only a small one) is predicted for models with $Z = 0.001$ and 0.004. On the other hand, models by Ventura et al., with $Z = 0.001$ and 0.004, show O enrichment in stars with ZAMS initial masses from 1.5 to 3.5 $M_\odot$.

Thus, in comparison with models and considering that the metallicity of H II regions in NGC 3109 is $Z \sim 0.0015$ (corresponding to 0.13 $Z_\odot$ if solar values by Asplund et al. 2005 are assumed), we found that the observed O enrichment in PNe of this galaxy is better reproduced by Ventura et al. models with $Z = 0.001$, and that the central stars of PNe have initial masses, at the ZAMS, from 1.5 to 3 $M_\odot$.

4.2. N/O abundance ratios

Figure 6 (left and right panels) shows the observed values of log (N/O) as a function of $12 + \log$ (O/H) for PNe (black dots) and H II regions (open squares). In comparison with the H II regions, the O enrichment of PNe mentioned above is evident. In addition, all PNe with available data, are N rich relative to H II regions by a factor of 10 in average. Extreme N enrichment is obtained in PN13, which has a N/O larger than 0.8 and is also very He rich, therefore it corresponds to a Peimbert Type I PN. In principle PNe with the most massive central stars,
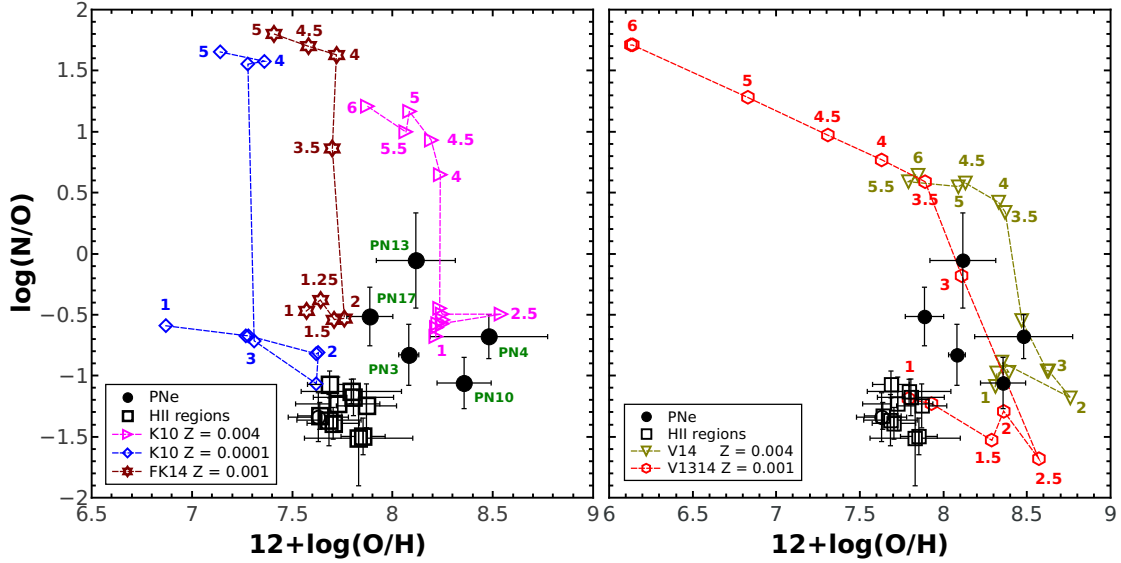
Fig. 6. log(N/O) versus 12 + log(O/H) for PNe (black dots), and H II regions (squares). The open circle corresponds to PN20, reclassified as a H II region. In the *left panel*, stellar evolution models for different metallicities by Karakas (2010, K10; $Z = 0.0001$, blue diamonds; $Z = 0.004$, magenta triangles) and Fishlock et al. (2014, F14; $Z = 0.001$, brown stars) have been included. In each metallicity sequence initial masses (at the ZAMS) of the progenitor stars are labeled for some models. In the *right panel* stellar evolution models for $Z = 0.001$ (red diamonds) by Ventura et al. (2013, 2014b, V1314) and $Z = 0.004$ (blue triangles) by Ventura et al. (2014a, V14) have been included. Again initial masses (at the ZAMS) of the progenitor stars are labeled for some models.
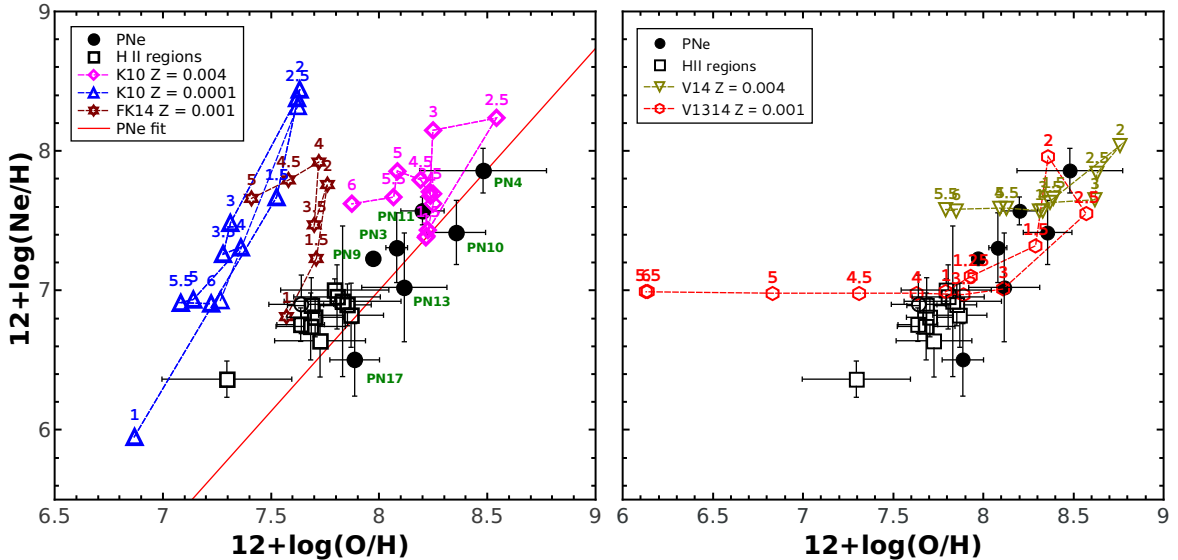
Fig. 7. 12 + log(Ne/H) versus 12 + log(O/H) for PNe (dots), and H II regions (open squares). Same stellar evolution models as in Fig. 6 have been included. In the *left panel* K10 models, with $Z = 0.0001$ (blue diamonds) and $Z = 0.004$ (magenta triangles), and FK14 models, with $Z = 0.001$ (brown stars), are presented. In the *right panel* models V1314 ($Z = 0.001$, red diamonds) and V14 ($Z = 0004$, green triangles) are shown. The ZAMS initial masses of the progenitor stars are labeled for some models in each metallicity sequence.

$M_\odot \geq 3\,M_\odot$, produce extra N enrichment by experiencing HBB, and this should be the case for PN13.

In Fig. 6, left panel, we show the behavior predicted by the stellar evolution models by K10 and F14 for metallicities $Z = 0.0001$, 0.001, and 0.004. In each metallicity sequence some models have been tagged with the ZAMS initial masses of stars. In this figure, it is found that our PNe lie nearer the models with metallicity $Z = 0.004$, which is in disagreement with the fact that the metallicity in NGC 3109 is about 0.0015. This occurs because models by F14 ($Z = 0.001$) and K10 ($Z = 0.004$) do not show O enrichment. In contrast, all these models predict that stars with initial masses larger than 2.5 $M_\odot$ produce large

amounts of N, similar to the value shown by our Type I PN. According to the models, PN13 central star would have had an initial mass of about 3.5 $M_\odot$. However, K10 and F14 models do not reproduce the low N/O abundance ratio of PN3 and PN10.

In the right panel of Fig. 6 we explore the behavior of log (N/O), in comparison with the stellar evolution models by Ventura et al. (2013, 2014b, V1314), for $Z = 0.001$ and Ventura et al. (2014a, V14), for $Z = 0.004$. For the same progenitor stars, these models predict lower N/O ratios than the models by K10 and F14. Within uncertainties, our objects follow more closely models V1314, with $Z = 0.001$, which predict O enrichment for stars with initial masses, at the ZAMS, equal

or larger than 1.5 $M_\odot$. However V1314 models predict very low N/O abundance ratios for stars with masses between 1.5 and 2.5 $M_\odot$. N enrichment in V1314 models occurs only for stellar masses larger than 2.5 $M_\odot$. According to these models, our PNe would have had initial masses larger than 2.5 $M_\odot$ and the progenitor of our Type I PN (PN13) would have had initial mass of about 3.5 $M_\odot$. Models V14, with metallicity $Z = 0.004$, show O abundances that are too large compared to our objects.

Hence, regarding N/O abundance ratios, all the model sequences analyzed here seem inadequate as compared with our data.

4.3. Ne/O abundance ratios

Values of Ne/H versus O/H abundances for PNe and H II regions are presented in Fig. 7. It is interesting to note that PN17 shows the lowest O and Ne abundances, similar to the values of H II regions, while all the other PNe present higher O and Ne abundances.

A tight correlation is found between Ne and O abundances similar to that found in all other sample of PNe and H II regions (Henry 1989; García-Hernández & Górny 2014; García-Rojas et al. 2016). The linear fit for PNe is $12 + \log(\text{Ne/H}) = (1.74 \pm 0.49) \times (12 + \log(\text{O/H})) - (6.60 \pm 4.05)$, with $R^2 = 0.70$. Thus, we have found that O is enriched in our PN sample, but given the slope of 1.74 in the log Ne/H versus log O/H diagram, Ne is even more enriched. This is a very important result that supports the chemical evolution models predicting large Ne enhancements for stars with very low metallicity and initial masses between 1.5 and 4 $M_\odot$ (Karakas & Lattanzio 2003).

In the left panel of Fig. 7, we present the predictions of stellar evolution models by K10 and F14 for $Z = 0.0001$, 0.001, and 0.004. As in Fig. 6, some ZAMS initial masses have been tagged in each sequence of metallicity. All the models predict large Ne increments, although they do not predict large O enrichment. Such large Ne increments occur for stars with initial masses between 1.5 and 4 $M_\odot$, depending on Z. Ne increments are mainly due to the enrichment of the ^{22}Ne isotope. In these models the usually most abundant isotope, ^{20}Ne, is not significantly modified by nucleosynthesis, but during the AGB phase; the ^{22}Ne abundance highly increases by means of two α-capture of ^{14}N, which transforms it into ^{22}Ne. Such a recently produced ^{22}Ne could be brought to the surface during third dredge-up events, increasing the total Ne abundance (Karakas & Lattanzio 2003).

In the models, stars with higher masses are less efficient in Ne enrichment because ^{22}Ne diminishes as a consequence of an α capture that destroys it; thus, in Fig. 7, the evolution traces at a given metallicity are bent over themselves.

In the left panel Fig. 7, several of our PNe lie near the models with $Z = 0.004$ which again is in disagreement with the metallicity in NGC 3109. Besides that, Ne in PN3, PN9, and PN13 is better reproduced by $Z = 0.001$ models, although O is not, and no model reproduces the low Ne abundance shown by PN17. Models with $Z = 0.001$ predict that the initial masses of the PN central stars would have been in the range from 1 to 4.0 $M_\odot$, while models with $Z = 0.004$ indicate that the initial masses were in the range from 1 to 2.5 $M_\odot$. PN4 has the largest Ne abundance and, according to $Z = 0.004$ models, its initial mass was about 2.0−2.5 $M_\odot$.

In the right panel of Fig. 7, we explore the Ne/H versus O/H behavior predicted by models by V1314 for $Z = 0.001$ and V14 for $Z = 0.004$. Our objects lie near models with $Z = 0.001$. The

observed Ne abundances are consistent with models for progenitors with initial masses of 1.25−3.5 $M_\odot$, but again no model predicts the low Ne found in PN17. In comparison with V1314 models, our Peimbert Type I PN13 would have had an initial mass of 3 $M_\odot$ while the extreme Ne-rich PN4 would have had an initial mass of about 2−2.5 $M_\odot$.

In conclusion, regarding the Ne/H versus O/H behavior, we find that V1314 models ($Z = 0.001$) agree better with our data, except for PN17, while F14 models ($Z = 0.001$) do not reproduce our PN data, as they predict too large Ne enrichment and too low O enrichment.

4.4. S and Ar abundances

Ar/H and S/H versus O/H abundances, for PNe and H II regions, are presented in Fig. 8 (left and right panels). In this graphs there are only a very few PNe with Ar and S abundance determinations and the uncertainties are large. No correlation with O is found for these α elements. Given the uncertainties, it is apparent that Ar and S abundances in PNe are similar to the abundances in H II regions.

Therefore, as expected, S and Ar are not enriched in PNe, and their values seems to correspond to a relatively young PN population.

4.5. Abundances in H II regions and chemical gradients

In Table 7 the chemical abundances for 11 H II regions, spreading over the entire region covered by the stars in the galaxy, are presented. It is evident that these young nebulae have remarkable uniform abundances, with an average $12 + \log \text{O/H}$ of 7.74 ± 0.09; the lower limit for H II 4 was not considered. Therefore we can conclude that the ISM, in the central 5 kpc of this galaxy is chemically homogeneous. This homogeneity of the ISM is consistent with similar results in other irregular galaxies like the Magellanic Clouds (Pagel et al. 1978; Dufour 1984), NGC 6822 (Hernández-Martínez et al. 2009) and others. Considering all these examples, a nearly constant O abundance is expected for irregular galaxies, and this is found over the optical extension of NGC 3109. To illustrate this fact, we present Fig. 9 where O abundances for H II regions and PNe are shown versus distance to the galactic center. No gradient is appreciated in H II regions, nor in PNe, from the center up to a radius of 2.5 kpc.

5. Is there a relation between the kinematics and chemistry in NGC 3109?

As it described above and shown in Fig. 9, there is no chemical gradient for H II regions in NGC 3109. PNe show no gradient either, but this is expected as the central stars modified their original O abundance. A chemical gradient was not found by Evans et al. (2007) and Hosek et al. (2014) either in their analysis of the chemistry of supergiant stars.

Therefore all the material in the bar of the galaxy, which is rotating with a velocity gradient of about 17 km s^{-1} per kpc, seems well mixed (possibly due to the action of the bar). This material includes the presence of a very young population represented by H II regions, which is a slightly older population represented by the supergiant stars and an intermediate-age population represented by the PNe. The latter two are distributed in a thicker zone than the H II regions.

As mentioned before, the lack of chemical gradients is usually found in irregular galaxies where different populations,
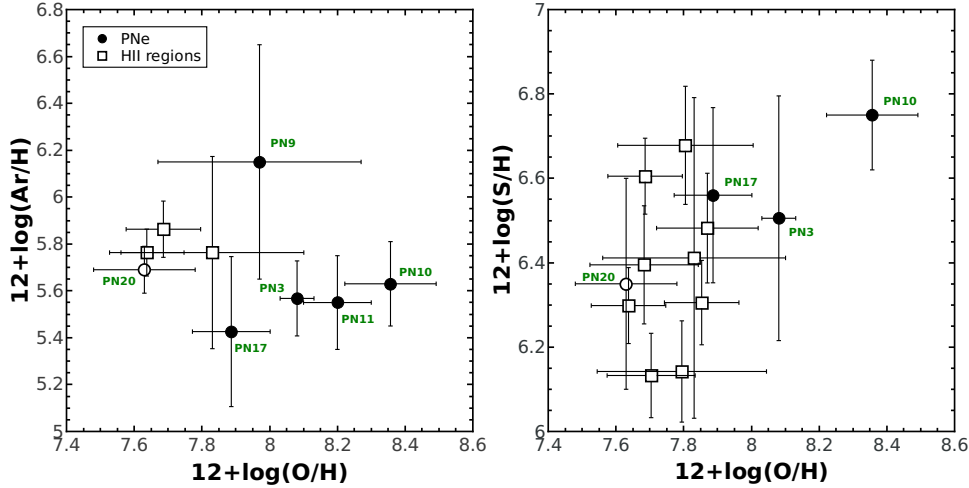
Fig. 8. 12 + log(Ar/H) versus 12 + log(O/H) and 12 + log S/H versus 12 + log(O/H) for PNe (dots), and H II regions (open squares).

often with different kinematics, are frequently found. This absence of a chemical gradient in irregular galaxies is contrary to what occurs in large spiral galaxies like the Milky Way, Andromeda, M 81, NGC 300, and others, where abundance gradients are clearly detected (Stasińska et al. 2013; Stanghellini et al. 2014, 2015; Magrini et al. 2016). The same authors have discussed the behavior of chemical gradients of H II regions in comparison with the gradients presented by PNe, finding that the latter are flatter than those presented by H II regions. They have attributed such a phenomenon to possible migration of PNe along the galactic disks.

It is interesting to mention here the situation in dwarf spheroidal (dSph) galaxies of the Local Group. Galaxies such as Fornax, Sculptor, Carina and Sextans have been analyzed and all of them display evidence for the coexistence of two or more populations with different metallicities (metal poor and metal rich), different spatial distribution, and different velocity dispersion profiles (see Zhu et al. 2016, and references therein). Chemodynamical models for some of these galaxies reveal that the dSphs have undergone different episodes of star formation in the past, the youngest of which gave origin to a richer population that is more centrally concentrated.

In NGC 3109 we are witnessing different episodes of star formation. Previous episodes generated the C-stars, PN central stars, and BSG stars, and the present episodes has generated OB stars ionizing H II regions. These populations (PNe, BSGs, and H II regions) apparently show slightly different dynamics (see Fig. 5) but not chemical gradients. In the irregular galaxy NGC 6822 different populations have also been found and in this case these populations do show different dynamics and different chemical composition, although no chemical gradients (Hernández-Martínez et al. 2009; Flores-Durán et al. 2014; García-Rojas et al. 2016).

Thus, it can be inferred that dwarf galaxies (spheroidals and irregulars) display in general complex structures that have several populations with different metallicities and dynamics. However no chemical gradients are evident in them. In the case of NGC 3109 deeper studies are needed to analyze the faint (presumable) old population to verify its metallicity and kinematics.

6. General conclusions

We study the kinematics of eight confirmed PNe and several H II regions that are distributed all over the entire region covered
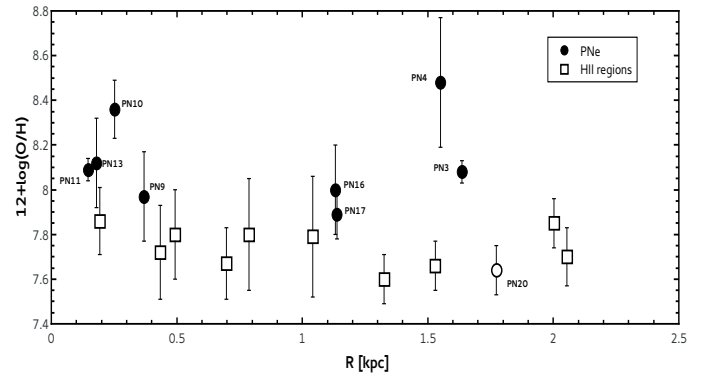

Fig. 9. O abundances of H II regions and PNe versus distance to the galactic center.

by stars in NGC 3109 using high spectral-resolution data obtained at OAN-SPM and LCO. The analyzed PNe represent more than 40% of the total sample of PN candidates known for this galaxy.

The kinematics of all these objects was analyzed in comparison with the kinematics of the huge H I disk that surrounds this galaxy. In addition, the kinematics of the blue supergiant stars (BSGs) of NGC 3109, as presented by Evans et al. (2007), was included in the analysis.

Our results show that H II regions share the H I gas kinematics with a dispersion velocity that is lower than 8.6 km s^{-1}. This is in agreement with the analysis of the ionized gas made by Blais-Ouellette et al. (2003). The rotation curve of these elements corresponds to that of a bar in the central zone of the galaxy. On the other hand, PNe and BSGs, even when they rotate in the same direction, show a very large dispersion in velocities. These objects could be even rotating with a slightly steeper rotation curve, although the low dispersion of data of BSGs prevents us from a conclusive result. This probable difference in kinematics, together with the fact that the distribution of PNe and BSGs corresponds to a thicker zone than the distribution of H II regions, indicates that these young and intermediate-age objects (BSGs and PNe) belong to different populations.

Using our observations with MIKE at LCO and the line intensities reported by Peña et al. (2007b), physical conditions and chemical abundances for the PNe were calculated using Delgado-Inglada et al. (2014) ICFs. No big differences in

abundances for O, N, and Ne were found using K&B94 or Delgado-Inglada et al. (2014) ICFs. Therefore in the cases where ICFs by Delgado-Inglada et al. (2014) cannot be used for these elements, we employed K&B ICFs. Chemical abundances in H II regions were also derived using K&B ICFs.

Our results reinforce that in NGC 3109, PNe are O enriched, relative to the H II regions, by an amount in average of 0.41 dex. This is important evidence that supports predictions of some stellar evolution models for low-intermediate mass stars, which indicate O enrichment at very low metallicity. It is worth mentioning that this is not the case in the more enriched galaxy NGC 6822, where PNe show O/H abundances in a large range, some being O richer and some O poorer than H II regions (García-Rojas et al. 2016).

In addition to O enrichment, we found that all but one of the observed PNe in NGC 3109 show Ne enrichment; this is in agreement with predictions of stellar evolution models, where total Ne is enriched via ^{22}Ne. This isotope can be nucleosynthesized through two α-capture of ^{14}N and brought to the surface by a third dredge-up episode in low-metallicity stars of ZAMS initial masses of $2-4$ $M_\odot$.

We compare our data with models by Karakas (2010), Fishlock et al. (2014), and nonstandard models by Ventura et al. (2013, 2014a,b) for different metallicities. It is found that the best agreement, for O and Ne abundances happens, concerning nonstandard models by Ventura et al. (2013, 2014a) at $Z = 0.001$, because at the metallicity of NGC 3109 ($Z \sim 0.0015$) models by Karakas (2010) and Fishlock et al. (2014) predict very low O enrichment and excess of Ne enrichment. A similar result was found for NGC 6822, where García-Rojas et al. (2016) found that Karakas (2010) models predicted excess of Ne in comparison with observations while models by Ventura agree better with data.

All the analyzed PNe present N enrichment. From the comparison of the PN N/O abundance ratios with the stellar evolution models cited above, it is found that the models fail in different ways. Karakas (2010) and Fishlock et al. (2014) models predict too much N/O (probably because they do not predict O enrichment) while Ventura et al. (2013, 2014a,b) models predict too low N/O values for stars with masses between 1.5 and 2.5 $M_\odot$. Therefore regarding N/O abundance ratios, the models analyzed here are inadequate. In order to build better models to reproduce PN observations it would be necessary to improve the yields for N. For the case of Ne, the inclusion of nonstandard effects like those by Ventura et al. (2013, 2014a,b) models helps to reproduce better the observational data.

Sulfur and argon were determined in a few PNe of our sample, which show abundances similar to the values in H II regions in NGC 3109. That is, contrary to N, O, and Ne, these two α elements show the original values at the moment of formation of the PN central stars. They could therefore be used instead of oxygen or neon as good tracers of chemical evolution with time.

One PN (PN17) in our sample has a very low Ne abundance. No evolution model predicts such a low Ne abundance at the metallicity of NGC 3109. This PN does not show large O enrichment either, therefore, it seems possible that such an object belongs to an older PN population or has a progenitor with an initial mass of about 1 $M_\odot$.

As derived from the spectroscopy, the PN candidate PN20 presented by Peña et al. (2007a) resulted to be a H II region and it was reclassified.

The abundances in H II regions were analyzed searching for a possible abundance gradient in the central zone of NGC 3109. No abundance gradient was found neither in NGC 3109 nor

in the supergiants stars analyzed by Evans et al. (2007) and Hosek et al. (2014). Therefore, even when NGC 3109 presents several different populations showing different chemistry and possibly different kinematics, no chemical gradient is found; this is similar to what occurs in other irregular galaxies of the Local Group, where very different populations exist (stellar clusters, old and young stars, H II regions, etc.) showing different kinematics, but no evidence for a chemical gradient is found.

As a result of this work we find that the predicted O, N, and Ne enrichment in PNe should be analyzed more deeply in stellar evolution models. The different models explored here agree in some aspects with the results of observations and disagree in others. In particular O enrichment should be reconsidered because some PNe in the solar vicinity, with carbon-rich dust, have shown such an O enrichment, by about 0.3 dex, compared to the H II regions in the same vicinity (Delgado-Inglada et al. 2015).

References

Asplund, M., Grevesse, N., & Sauval, A. J. 2005, in Cosmic Abundances as Records of Stellar Evolution and Nucleosynthesis, eds. T. G. Barnes, III, & F. N. Bash, ASP Conf. Ser., 336, 25

Barnes, D. G., & de Blok, W. J. G. 2001, AJ, 122, 825

Berstein, R. A., Shectman, S. A., Gunnels, S., Mochnacki, S., & Athey, A. 2002, Proc. SPIE, 4841, 1694

Blais-Ouellette, S., Amram, P., & Carignan, C. 2003, ApJ, 121, 1952

Bresolin, F., Capaccioli, M., & Piotto, G. 1993, AJ, 105, 1779

Carignan, C., Frank, B. S., Hess, K. M., et al. 2013, AJ, 146, 48

Coccato, L., Gerhard, O., Arnaboldi, M., et al. 2009, MNRAS, 394, 1249

Cortesi, A., Arnaboldi, M., Coccato, L., et al. 2013, A&A, 549, A115

de Vaucouleurs, G., de Vaucouleurs, A., Corwin, H. G., et al. 1991, Third Reference Catalogue of Bright Galaxies (Berlin, Heidelberg, New York: Springer-Verlag)

Debattista, V. P., & Sellwood, J. A. 2000, ApJ, 543, 704

Delgado-Inglada, G., Morisset, C. & Stasińska, G. 2014, MNRAS, 440, 536

Delgado-Inglada, G., Rodríguez, M., Peimbert, M., Stasińska, G. & Morisset, C. 2015, MNRAS, 449, 1797

Demers, S., Battinelli, P. & Letarte, B. 2003, A&A, 410, 795

Dufour, R. J. 1984, in Structure and evolution of the Magellanic Clouds, IAU Symp., 108, 353

Evans, C. J., Bresolin, F., Urbaneja, M. A., Pietrzyński, G., & Gieren, W. 2007, ApJ, 659, 1198

Fishlock, C. K., Karakas, A. I., Lugaro, M., & Yong, D. 2014, ApJ, 797, 44

Flores-Durán, S. N., Peña, M., Hernández-Martínez, L., et al. 2014, A&A, 568, A82

García-Hernández, D. A., & Górny, S. K. 2014, A&A, 567, A12

García-Rojas, J., Peña, M., Flores-Durán, S., & Hernández-Martínez, L. 2016, A&A, 586, A59

Gonçalves, D. R., Teodorescu, A. M., Alves-Brito, A., Méndez, R. H., & Magrini, L. 2012, MNRAS, 425, 2557

Henry, R. B. C. 1989, MNRAS, 241, 453

Herrmann, K., & Ciardullo, R. 2009, ApJ, 705, 1686

Hernández-Martínez, L., Peña, M., Carigi, L., & García-Rojas, J. 2009, A&A, 505, 102

Hodge, P. W. 1969, ApJS, 18, 73

Hosek Jr., M. W., Kudritzki, R.-P., Bresolin, F., et al. 2014, ApJ, 785, 151

Jobin, M., & Carignan, C. 1990, AJ, 100, 3

Karakas, A. I. 2010, MNRAS, 403, 1413

Karakas, A. I., & Lattanzio, J. C. 2003, Publ. Astron. Soc. Aust., 20, 393

Kingsburg, R. L., & Barlow, M. J. 1994, MNRAS, 271, 257

Longobardi, A., Arnaboldi, M., Gerhard, O., et al. 2013, A&A, 558, A42

Magrini, L., Coccato, L., Stanghellini, L., Casasola, V., & Galli, D. 2016, A&A, 588, A91
Marigo, P. 2001, A&A, 370, 194
McConnachie, A. W. 2012, AJ, 144, 4
Meaburn, J., Blundell, B., Carling, R., et al. 1984, MNRAS, 210, 463
Meaburn, J., López, J. A., Gutiérez, L., et al. 2003, Rev. Mex. Astron. Astrofis., 39, 185
Merrett, H. R., Merrifield, M. R., Douglas, N. G., et al. 2006, MNRAS, 369, 120
Minniti, D., Zijlstra, A. A., & Alonso. V. M. 1999, AJ, 117, 881
Ott, J., Stilp, A. M., Warren, S. R., et al. 2012, AJ, 144, 123
Pagel, B. E. J., Edmunds, M. G., Fosbury, R. A. E., & Webster B. L. 1978, MNRAS, 184, 569
Peña, M., Richer, M. G, & Stasińska, G. 2007a, A&A, 466, 75
Peña, M., Stasińska, G., & Richer, M. G. 2007b, A&A, 476, 745
Richer, M. G., & McCall, M. L. 1992, AJ, 103, 54

Richer, M. G., López, J. A., Díaz-Méndez, E., et al. 2010, Rev. Mex. Astron. Astrofis., 46, 191
Seaton, M. 1979, MNRAS, 187, 73
Soszynśki, I., Gieren, W., Pietrztyński, G., et al. 2006, ApJ, 648, 375
Stanghellini, L., Magrini, L., Casasola, V., & Villaver, E. 2014, A&A, 567, A88
Stanghellini, L., Magrini, L., & Casasola, V. 2015, ApJ, 812, 39
Stasińska, G., Peña, M., Bresolin, F., & Tsamis, Y. G. 2013, A&A, 552, A12
Storey, P. J., & Hummer, D. G. 1995, MNRAS, 272, 41
Valenzuela, O., Rhee, G., Anatoly, K., et al. 2007, ApJ, 657, 773
Ventura, P., Di Criscienzo, M., Carini, R., & D'Antona, F. 2013, MNRAS, 431, 3642
Ventura, P., Di Criscienzo, M., D'Antona, F., et al. 2014a, MNRAS, 437, 3274
Ventura, P., Dell'Agli, F., Schneider, R., et al. 2014b, MNRAS, 439, 977
Weinberg, M. D. 1985, MNRAS, 213, 451
Zhu, L., van de Ven, G., Watkins, L. l., & Posti, L. 2016, MNRAS, 463, 1117